Perovskite-oxide based hyperbolic metamaterials

Mohamed Bouras, Dong Han, Sébastien Cueff, Romain Bachelet, Guillaume Saint-Girons

Perovskite-oxide based hyperbolic metamaterials

*Mohamed Bouras, Dong Han, Sébastien Cueff, Romain Bachelet and Guillaume Saint-Girons**

Institut des Nanotechnologies de Lyon, INL-CNRS/UMR5270, Ecole Centrale de Lyon, 36 avenue Guy de Collongue FR 69134 Ecully cedex, France.

Keywords : Hyperbolic Metamaterials, Functional Oxides, Perovskite, Molecular Beam Epitaxy, Plasmonic Materials

Abstract

We show that conducting $La_xSr_{1-x}TiO_3$ (LSTO) presents excellent plasmonic properties in the near- to mid-infrared region, and that these properties can be tuned with unrivalled flexibility by controlling the La composition. Taking advantage of this outstanding plasmonic response, we demonstrate a new class of hyperbolic metamaterials (HMMs) composed of LSTO/$SrTiO_3$ (STO) epitaxial superlattices showing a high figure of merit in a spectral range not currently available with other known HMMs. The epitaxial nature of these HMMs combined with the tunability of the LSTO plasmonic response provides ultimate control on their dielectric properties, including their hyperbolic wavelength range. The epitaxial coherency and atomic level abruptness of the LSTO/STO interfaces supporting the plasmon resonances contribute to their low absorption losses. These HMMs involve individual layers with very low thicknesses (few nanometers), and can be combined by epitaxy to the many members of the functional oxide family, opening perspectives

for their very compact integration in multifunctional heterostructures. They can also be epitaxially grown on Si and GaAs technological platforms by epitaxy using $SrTiO_3$/Si and $SrTiO_3$/GaAs templates, making them perfectly suited for versatile integration in nanophotonic devices

Hyperbolic metamaterials (HMMs) are uniaxially anisotropic multi-layered structures with dielectric permittivities of opposite signs depending on the structural direction ($\varepsilon_{r\text{-}o} < 0$ and $\varepsilon_{r\text{-}e} > 0$, or $\varepsilon_{r\text{-}o} > 0$ and $\varepsilon_{r\text{-}e} < 0$, where $\varepsilon_{r\text{-}o}$ and $\varepsilon_{r\text{-}e}$ designate the ordinary and extraordinary components of the dielectric function, respectively). This very strong anisotropy results from the alternation of dielectric and conductive layers along the extraordinary axis. It gives rise to unique optical properties, as reviewed in Ref. 1 and 2. For instance, such materials present negative refraction, enabling the design of hyperlenses for sub-wavelength imaging.[3,4] In addition, propagation in HMMs can theoretically occur with infinite wavevector which enables novel concepts for optical cavity design,[5] and allows for developing novel promising strategies of photonic density of states engineering.[6] HMMs have also been identified as very efficient thermal emitters.[7] These materials have thus established themselves as essential elements of the toolkit for photonic device design.

HMMs properties (recently reviewed in Ref. 8 and 9) depend to a large extent on that of the plasmonic conductive material inserted in the superlattice, and in particular on its cross-over frequency, above which the real part of its permittivity is negative due to the Drude contribution associated to the free carriers, and on its optical losses that must be minimal.[10] Metals (silver, gold) have excellent properties in the UV and visible range, and are used in classical HMMs in alternation with SiO_2 or TiO_2 dielectric layers.[8,11,12] Such HMMs are very effective in the ultraviolet range and up to the visible region, but are limited by metal optical losses at longer wavelengths. [9,13,14,15,16] In the mid-infrared region, for wavelengths larger than 6-8 µm, doped III-V semiconductors such as InGaAs have excellent plasmonic properties.[10,15,17] HMMs based on these materials (such as InAlAs/InGaAs superlattices epitaxially grown on InP substrates[17]) show excellent figure of merits in this spectral range. At lower wavelength, between 4.5 and 8 µm, hyperbolicity has been achieved using graphene/Al_2O_3 superlattices.[18] In the near infrared region,

transparent conductive oxide (TCO) such as indium-tin oxide (ITO), and Al or Ga doped ZnO (respectively AZO and GZO) present the best plasmonic properties reported to date.[10] Hyperbolicity has been observed between 1.5 and 2 μm using TCO based HMMs.[19,20] In the same range, SiC- or metal nitrides-based HMMs have also been reported.[21,22] There is thus a gap between approximately 2 and 4.5 μm where hyperbolicity has to date not been demonstrated. However, this wavelength range is of significant technological importance for telecom and military applications, as it broadly overlaps the 3-5 μm atmospheric window.

Besides, flexibility to control the permittivity and hyperbolicity of HMMs is of utmost importance, so that they can be custom-made to fulfill the specifications of the device in which they are integrated.[9] In this regard, the approaches mentioned above are not of equal merit. Hence, the optical properties of HMMs based on metals are rigidly fixed by the non-modifiable transport properties of these materials. Higher flexibility is provided by the use of doped III-V semiconductors and TCO layers as conductive material, as their conductivity can be tuned by changing their doping level. The range over which the cross-over frequency can be modified is a relevant metric of their "plasmonic tunability".[10] This range lies in the > 6 μm for III-V semiconductors[10] (shorter wavelengths cannot be addressed due to the solubility limit of N-type dopants in these compounds,[23,24,25] and to the high effective mass typical for P-type doped III-V semiconductors[26]), between 1.38 and 1.55 μm for GZO and ITO, and between 1.8 and 3.5 μm for AZO.[10]

The electrical properties of conductive $La_xSr_{1-x}TiO_3$ (LSTO) are well documented in the literature,[27,28] and these compounds are also known for their low optical absorption.[29] We show here that this material presents excellent plasmonic properties in the near- to mid-infrared region, and we demonstrate a new class of HMMs, based on LSTO/$SrTiO_3$ (STO) epitaxial superlattices

and depicted in Fig.1, covering the 1.46 to 4.5 µm range substantially uncovered by any currently available HMMs.

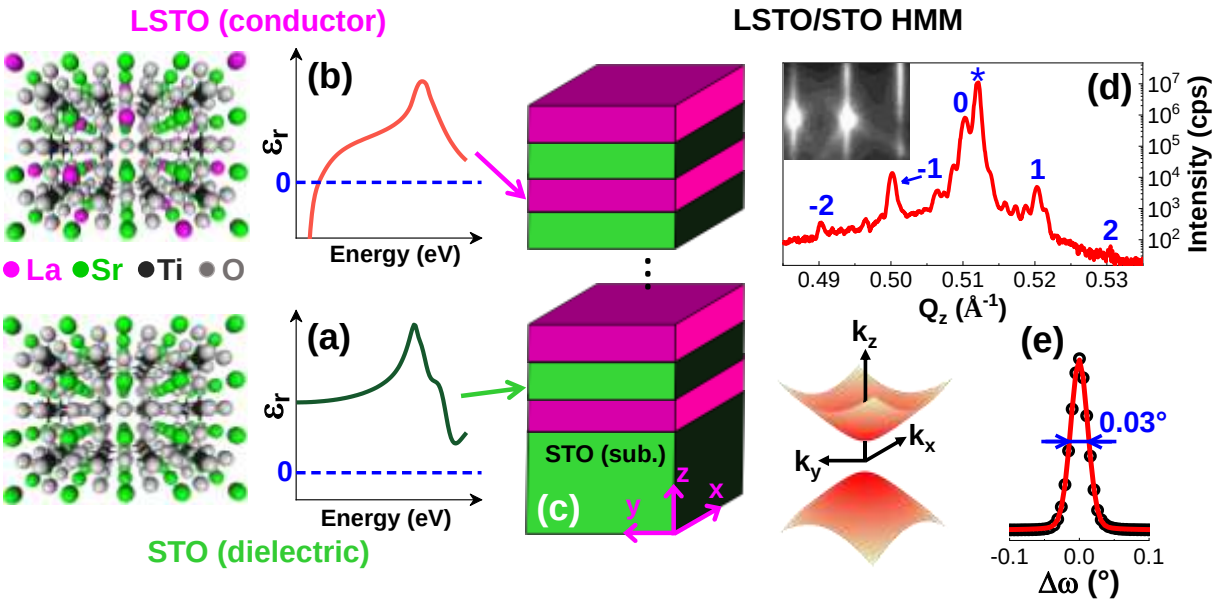

Figure 1. Whereas STO is a dielectric oxide with positive real permittivity ε_r (a), LSTO is conductive leading to negative ε_r in the infrared region due to free charge carriers (b). Epitaxial superlattices alternating STO and LSTO are thus expected to behave as HMMs (c). (d) X-ray radial scan recorded around the (002) reflection of such a superlattice (sample SL-20%-5nm, see Tab.1 for sample nomenclature). Q_z is the out-of-plane diffraction vector and * designate the STO (002) substrate reflexion. The presence of Pendellösung fringes and of well-defined superlattice satellite reflexions (indexed using blue numbers) attests for the excellent structural quality and single-crystallinity of the sample, further confirmed by the well-contrasted streak lines of the reflection high-energy electron diffraction (RHEED) pattern recorded at the end of sample growth (inset of (d)) and by the low full width at half maximum (0.03°) of the X-ray rocking curve recorded around the 0^{th} order satellite peak (e).

We also show that the cross-over frequency of LSTO layers can be tuned with unrivalled flexibility in the near to mid infrared region by varying the La concentration, which provides

considerable agility for adjusting the hyperbolic spectral range of the HMMs. Besides, the high crystalline quality and epitaxial nature of the LSTO/STO HMMs leads to atomic level abruptness and epitaxial coherency of the LSTO/STO interfaces supporting the plasmon resonances. We show that this, combined with the excellent plasmonic properties of the LSTO layers, enables achieving very high HMMs figure of merits.

The samples considered in the following were grown by MBE on undoped STO susbtrates according to the procedure described in the method section. They include LSTO layers (samples L-5%, L-10% and L-20%) and LSTO/STO superlattices (samples SL-20%-3nm, SL-20%-5nm, SL-20%-7nm and SL-10%-9nm) with different La concentrations. In the superlattice samples, the individual STO and LSTO layers are of equal thickness $t = \Lambda/2$, where Λ is the superlattice period. The La concentrations were estimated by XPS, the thicknesses of samples L-5%, L-10% and L-20% were measured using X-ray reflectivity (XRR) and ellipsometry, and the thicknesses of the superlattice samples were measured by X-ray diffraction (XRD) and ellipsometry (see the supporting information for more details). The sample characteristics are summarized in Tab.1.

Simple layers

Sample	%La *(XPS)*	Thickness (nm) *(XRR)*	*(ellipso)*
L-5%	**5** ± *1*	**17.0** ± *0.3*	**16.9** ± *0.8*
L-10%	**12** ± *1*	**15.6** ± *0.3*	**14.6** ± *0.4*
L-20%	**22** ± *1*	**23.7** ± *0.6*	**22.8** ± *0.2*

Superlattices

Sample	Period number	%La *(XPS)*	t = Λ/2 (nm) *(XRD)*	Thickness (nm) *(XRD)*	*(ellipso)*
SL-20%-3nm	**10**	**22** ± *1*	**2.94** ± *0.03*	**58.9** ± *0.7*	**61** ± *1.7*
SL-20%-5nm	**14.5**	**22** ± *1*	**4.95** ± *0.03*	**143.7** ± *0.8*	**144.2** ± *0.6*
SL-20%-7nm	**13.5**	**22** ± *1*	**7.23** ± *0.03*	**195.2** ± *0.8*	**199** ± *2.1*
SL-10%-9nm	**13**	**12** ± *1*	**9.52** ± *0.04*	**247** ± *1*	**248** ± *1*

Table 1. Nomenclature, compositions and thicknesses of the samples

Extensive structural characterizations carried out on the LSTO layer samples (Supporting Information, Fig.S1 and S2) attest for their good structural quality. Electrical and ellipsometric measurements were also carried out on these samples. The results are summarized in Fig.2.

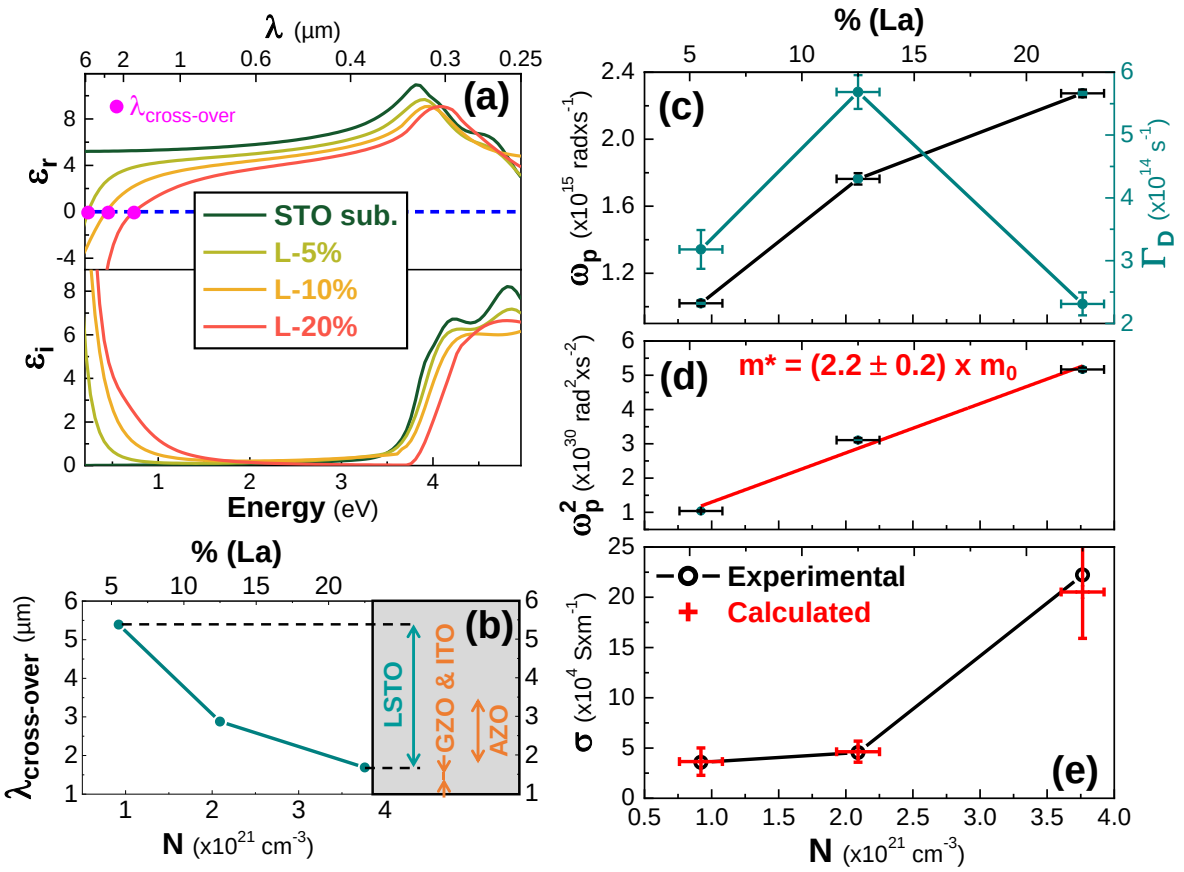

Figure 2. (a) : Real (ε_r) and imaginary (ε_i) parts of the dielectric function of the LSTO layers compared to that of a STO substrate (STO sub.) annealed in the MBE reactor in O_2 partial pressure and temperature conditions mimicking LSTO growth. (b) LSTO cross-over wavelength extracted from Fig.2(a) as a function of the charge carrier density N (assumed to be equal to the La atom concentration). Shaded block: cross-over wavelength range accessible by varying the charge carrier concentration for LSTO (blue), compared to that of plasmonic TCOs (from Ref. 10). (c) : Plasma frequency (ω_p, black) and friction coefficient (Γ_D, blue) of the Drude contributions to the

dispersions of the LSTO layers, as measured by ellipsometry, as a function of the charge carrier density. (d) ω_p^2 varies linearly with N within experimental accuracy. The electron effective mass m* extracted from the slope (red line) using Eq.1 is $(2.2 \pm 0.2) \times m_0$, where m_0 is the electronic mass. (e) Conductivity σ as a function of N, deduced from Hall measurements (black circles) and calculated by introducing the values of m^* and Γ_D (red error bars, deduced from ellipsometry) in Eq.2. The good match between measured and calculated values illustrates the consistency of the measurements.

The dielectric functions of the LSTO layers (measured by ellipsometry as detailed in the supporting information) displayed in Fig.2(a) present a Drude contribution leading to negative ε_r above the cross-over wavelength $\lambda_{cross\text{-}over}$, in the near- to mid-infrared region. Profitably for HMMs design, changing the La concentration allows for tuning $\lambda_{cross\text{-}over}$ over a very wide range, much wider than that achievable using TCOs, as shown in Fig.2(b). This is due to some specificities of LSTO. In these solid solutions, trivalent La substitutes divalent Sr on lattice sites, so that each La atom releases one electron in the structure.[30] LSTO is thus a N-type conductor for La compositions up to 25-30%, with a charge carrier concentration very close to the La atom concentration, extendable up to 10^{22} cm^{-3}. [28,30,31,32,33,34,35] Interestingly, LSTO solid solutions are stable and crystallize perfectly in the perovskite lattice structure over the entire N-type range (up to 30% La)),[36,37] so that increasing the charge carrier concentration in this region by increasing the La concentration does degrade neither the crystal structure, nor the room temperature charge carrier mobility.[34,38] This contrasts with the observations reported for plasmonic TCOs.[39]. Hence, for AZO and GZO, charge carrier concentrations up to 10^{21} cm^{-3} have been reported,[40,41] but the structural quality of these compounds degrades when the dopant concentration exceeds approximately 2-3% of Al or Ga, corresponding to a charge carrier concentration in the 10^{20} cm^{-3}

range,[39] which limits the "plasmonic tunabilty" of these materials as compared to that of LSTO. Regarding optical absorption in the $\lambda > \lambda_{cross\text{-}over}$ region, it is very low in LSTO as compared to that of typical conductors used for HMMs fabrication : for sample L-20% for instance, ε_i decreases from 4 at 2 µm to 2.2 at 1.55 µm, much lower than that of Ag (around 20)[12] and that of TiN (around 15)[22] in the same wavelength range. These very low values are comparable to the state of the art values reported for AZO and GZO in this spectral region (namely 1 to 2).[20,22]

The plasma frequency ω_p and the friction coefficient Γ_D extracted from ellipsometry measurements are plotted in Fig.2(c). Fig.2(d) shows that ω_p^2 varies linearly with N, as expected from Drude model:[42]

$$\omega_p = \sqrt{\frac{N \times e^2}{\varepsilon_0 \times m^*}} \qquad \text{Eq.1}$$

where e the electron charge, ε_0 the vacuum permittivity and m^* the electron effective mass. This suggests that the electron effective mass in LSTO does not significantly depends on La concentration. Fitting Eq.1 to the experimental data of Fig.2(d) gives an estimation for m* to (2.2 ± 0.2)×m_0, where $m_0 = 9.11 \times 10^{-31}$ kg is the electronic mass. This value is comparable to that reported in the literature.[32] The evolution of LSTO conductivity σ with La concentration is plotted in Fig.2(e). In this figure, the black circles correspond to the values measured using Hall effect, and the red error bars correspond to the values calculated using the effective mass and the friction coefficients Γ_D extracted from ellipsometry measurements, according to the Drude model:[42]

$$\Gamma_D = \frac{N \times e^2}{\sigma} \qquad \text{Eq.2.}$$

The excellent match between experimental and calculated σ values attest for the consistency of the measurements. LSTO presents excellent conductivities, comparable to that of commercial Nb-doped substrates for the L-20% sample, and consistent with the values reported in the literature.[27,28]

These results show the potential of LSTO as tunable plasmonic material in the near- to mid-infrared region, thanks to a unique combination of high electric conductivity and low absorption losses.

We now discuss the properties of the LSTO/STO superlattices (samples SL-20%-3nm, SL-20%-5nm, SL-20%-7nm and SL-10%-9nm). X-ray diffraction and reflexion high energy electron diffraction (RHEED) analyses (summarized in Fig.1(d) and (e) for sample SL-20%-5nm and extensively reported in the supporting information for all the samples, Fig.S4 and S5) show that all superlattice samples are epitaxially grown on their substrates, with excellent crystallinity and low surface roughness. In particular, the presence of well-defined superlattice satellite peaks in the X-ray diffraction patterns of the samples attests for the abruptness of the STO/LSTO interfaces. Conditions of continuity of the electrical field and electrical displacement in superlattices imply that the latter can be described as equivalent anisotropic uniaxial media with an ordinary axis parallel to interface planes and an extraordinary axis perpendicular to the interface planes[43,44,45] (as sketched in Fig.3), on condition that the superlattice period Λ is much smaller than the wavelength. As this condition is verified over the entire experimental range considered here (the largest Λ value considered here, namely 19 nm for sample SL-10%-9nm, is more than ten times larger than the minimal ellipsometry measurement wavelength, namely 260 nm), the superlattices were considered as homogeneous uniaxially anisotropic media to fit the ellipsometry measurements (using the procedure detailed in the Supporting Information). The excellent match between model and experiment further supports this hypothesis (Fig.S7). The superlattice dispersions in the infrared region are plotted in Fig.3.

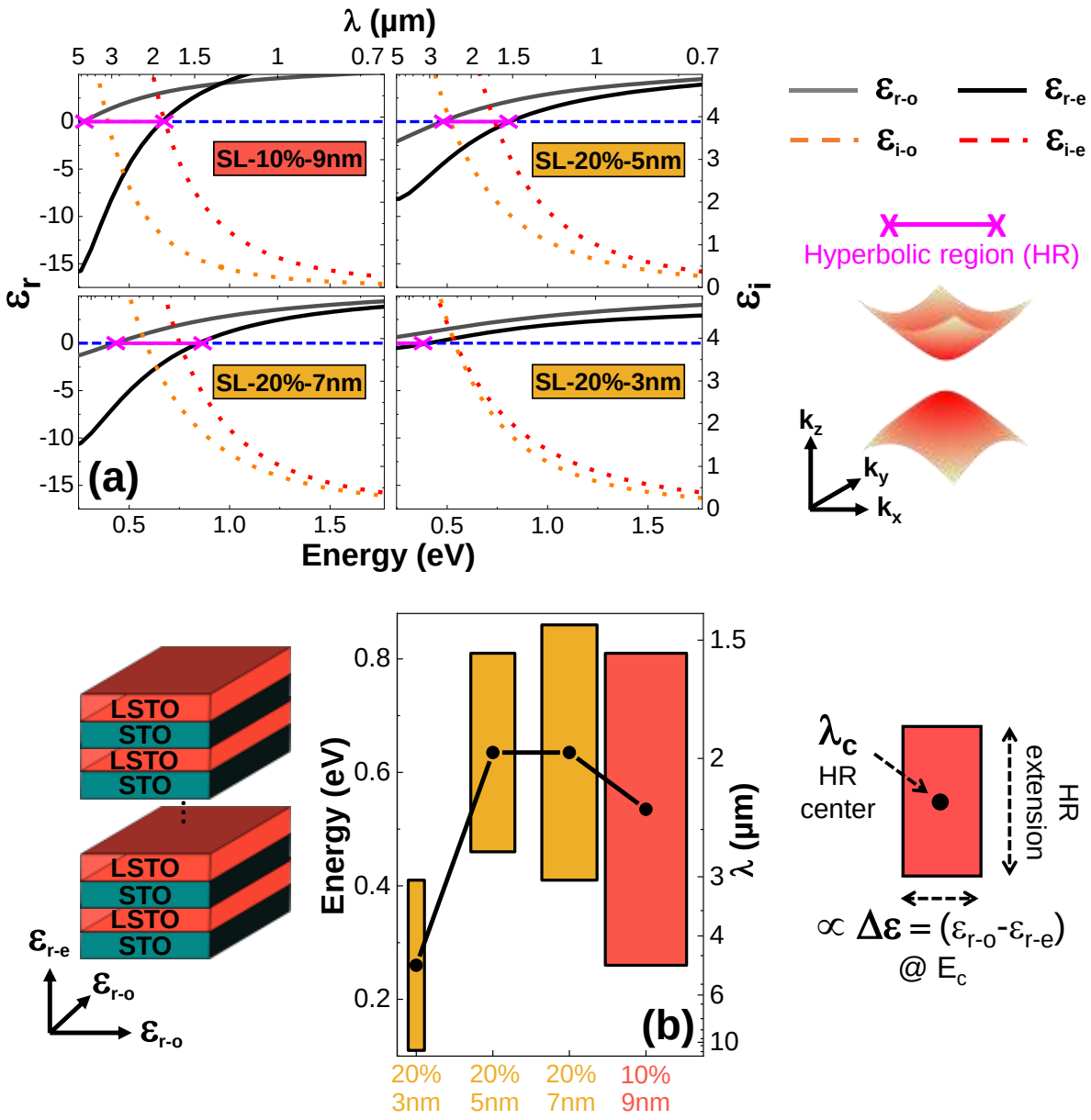

Figure 3. (a): Dispersions of the dielectric functions in the infrared region for the superlattice samples. Pink segments designate the type I hyperbolic regions (HR), where light propagation is described by hyperbolic isofrequency contours (Eq.3). (b): Spectral extension of the HR for the different samples. Black dots indicate the central energy of the HR (λ_c), and the width of the bars is proportional to the permittivity contrast $\Delta\varepsilon = (\varepsilon_{r\text{-}o} - \varepsilon_{r\text{-}e})$ measured at λ_c.

Type I HMMs behavior ($\varepsilon_{r\text{-}e} < 0$ and $\varepsilon_{r\text{-}o} > 0$) is observed in spectral regions indicated by pink arrows in Fig.3(a). In these regions, light propagation is described by hyperbolic isofrequency contours:[46]

$$\frac{k_x^2+k_y^2}{\varepsilon_{r-e}} + \frac{k_z^2}{\varepsilon_{r-o}} = \frac{\omega^2}{c^2}, \qquad \text{Eq.3}$$

where k_x, k_x, and k_x, are the components of the wavevector in the coordinate system sketched in Fig.3, ω is the angular frequency of the radiation and c the light velocity. Samples SL-10%-9nm and SL-20%-7nm are hyperbolic in wide spectral ranges, namely from 1.5 to 4.5 µm and from 1.46 to 3 µm, respectively. At first approximation, assuming perfectly abrupt transitions between the permittivity of the conductive layers (ε_{LSTO}) and that of the insulating layers (ε_{STO}) in the superlattices, the complex ordinary and extraordinary components of the superlattice permittivities read

$$\varepsilon_o = \frac{1}{1+\alpha} \times (\varepsilon_{LSTO} + \alpha \times \varepsilon_{STO}) \text{ and } \frac{1}{\varepsilon_e} = \frac{1}{1+\alpha} \times \left(\frac{1}{\varepsilon_{LSTO}} + \alpha \times \frac{1}{\varepsilon_{STO}}\right), \qquad \text{Eq.4}$$

and do not depend on the individual insulating and conductive layer thicknesses (d_{STO} and d_{LSTO}), but only on their ratio $\alpha = d_{LSTO}/d_{STO}$.[43,47] Under this very simplifying assumption, as $\alpha = 1$ for both SL-10%-9nm and SL-20%-7nm samples, the difference between the hyperbolic spectral ranges of these two samples would stem from the difference between the La concentrations in the LSTO layers. However, significant deviation from the behavior predicted by Eq.4, and in particular significant dependency of the equivalent permittivity to the individual layer thicknesses, is expected in cases where gradual transition between the permittivies of the conductive and insulating layers exist at the superlattice heterointerfaces.[44, 45, 48]. Such gradualness may be caused by interdiffusion or structural roughness at the interfaces, or by electronic effects such as coupling, charge transfer or charge accumulation at the interfaces. Whereas the structural characterizations

reported in Fig.1 indicate that interface interdiffusion or roughness may be discarded for our samples, several elements suggest that interface electronic effects should have significant impact on the HMM response. First, the very few reports available in the literature concerning LSTO band structure do not allow to discard significant difference between STO and LSTO bandgaps : the absorbance measurements reported in Ref.29 suggests that LSTO bandgap is in the 3.2-3.3 eV range, comparable or slightly larger than that of STO (3.22 eV[49]), for La concentrations up to 15%, and the calculations reported in Ref.50 predict an increase of LSTO bandgap with increasing La concentration, in keeping with our ellipsometry results (see Supplementary information, Tab.S2). Each STO/LSTO interface is thus liable to form a heterojunction where charge carriers can accumulate. Additionally, careful examination of the results depicted in Fig.3 suggests that they may not be properly described by Eq.4 : samples SL-20%-7nm, SL-20%-5nm and SL-20%-3nm present significantly different dispersions, whereas they all present the same La concentration and the same ratio α. Hence, Fig.3(b) highlights the strong dependency of the spectral extension of the hyperbolic region and of the permittivity contrast $\Delta\varepsilon = \varepsilon_{r\text{-}o} - \varepsilon_{r\text{-}e}$ (measured here at the central wavelength of the hyperbolic region) on the individual layer thickness: the hyperbolic window significantly narrows and $\Delta\varepsilon$ is strongly reduced when the individual layer thickness decreases, at constant α. This phenomenon is particularly acute for sample SL-20%-3nm, which presents the thinnest individual layers and a quasi-0 $\Delta\varepsilon$. In our superlattices, the conductive LSTO layers are separated by ultrathin (few nm thick) dielectric STO layers. Non negligible coupling between the surface plasmons supported by neighbouring LSTO/STO interfaces is thus liable to occur, affecting the overall response of the HMMs particularly for the samples with the thinnest individual layer thicknesses. Similarly, tunnel effect is expected to present significant contribution for STO thicknesses below 10 nm,[51] which may also impact the properties of the HMMs. Such

effects cause significant deviation from the behaviour predicted by Eq.4, and may besides by exploited to further engineer the dielectric response of HMMs.

The results depicted in Fig.3 show that La concentration can be used as an efficient lever to control hyperbolicity in LSTO/STO superlattices. They also show that all LSTO/STO HMMs present moderate ε_i values (ranging from 2 to 4) and thus low optical losses in their hyperbolic spectral regions. Actually, the performances of HMMs are commonly benchmarked using the so-called figure of merit for HMMs (FOM),[17,52] that can be deduced from dielectric functions using Eq.3 and is defined as :

$$FOM = \frac{Re(k_z)}{Im(k_z)} \text{ (calculated at } k_x = k_y = 0) \qquad \text{Eq. 5}$$

The FOM takes into account both the confinement efficiency of the HMMs (Re(k)) and its absorption losses (Im(k)), and is calculated for the wavevector component perpendicular to the sample surface, which experiences negative permittivity in the case of a type I HMMs. The FOM of samples SL-10%-9nm and SL-20%-7nm in the wavelength ranges where these samples present hyperbolic dispersions are compared in Fig.4 to that of typical metal based HMMs, and to state of the art values in this wavelength range.

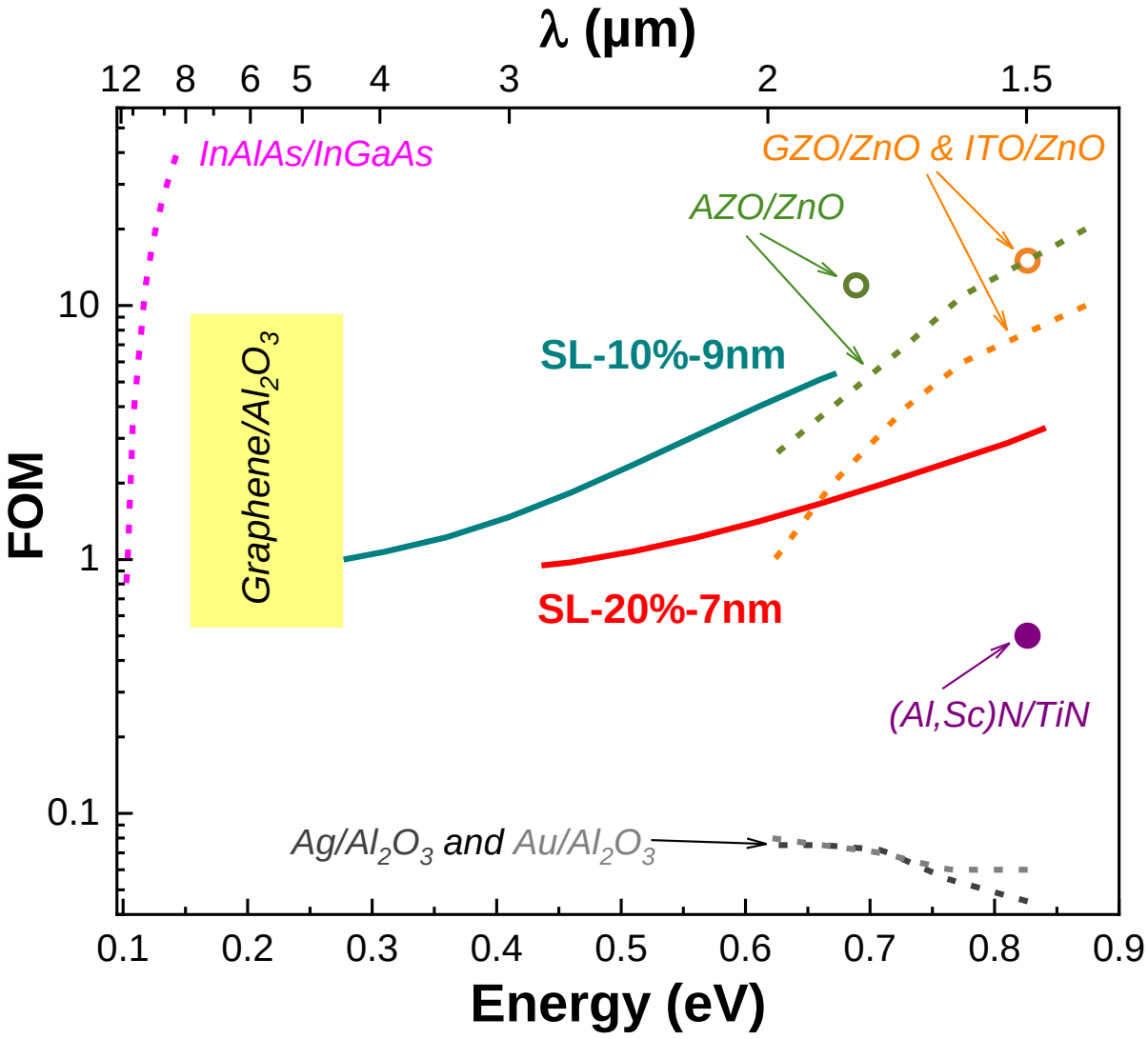

Figure 4. Figure of merits or samples SL-10%-9nm (continuous blue line) and SL-20%-7nm (continuous red line) in their hyperbolic spectral ranges, compared to state-of-the art values in this wavelength region from the literature : grey dashed lines : typical metal based HMMs,[20] purple circle : (Al,Sc)N/TiN HMMs,[53] green open circle and green dashed line : AZO/ZnO HMMs[10,20,54] , orange open circle : GZO/ZnO and ITO/ZnO HMMs[10,55] , and pink dashed line : InAlAs/InGaAs.[17] The yellow box indicate the spectral range where graphene/Al_2O_3 superlattices have been reported as hyperbolic,[18] and for which no data on FOM is available.

The FOM of samples SL-10%-9nm and SL-20%-7nm is in the 1 to 6 range between 1.46 and 4.5 µm, and is by far better than that of typical metal based HMMs or even than that of nitride based HMMs in comparable wavelength range. Up to approximately 1.8 µm, state-of-the-art AZO and GZO based HMMs outperform our samples, but at longer wavelength, the FOM of our samples present unrivalled values. Interestingly, LSTO/STO HMMs covers the gap between 2 and 4.5 µm in which no hyperbolic material was available so far. This confers on them strong applicative interest, as this wavelength range (1st atmospheric window) is of significant technological importance for telecom and military applications, as well as for atmospheric gas analysis and CO_2 detection.[56] In the end, the results presented here are a simple proof-of-concept of the flexibility offered by LSTO/STO superlattices to design HMMs. Indeed, tuning the La concentration in the full accessible alloying range is expected to lead to significant widening of accessible hyperbolic wavelength range, in particular towards longer wavelengths.

As a conclusion, our results show that conductive $La_xSr_{1-x}TiO_3$ (LSTO) layers present plasmonic properties competing with that of TCO and that these properties can be tuned with unrivalled flexibility in the near to mid infrared region. Based on this, we demonstrate a new class of HMMs in the IR range based on LSTO/STO superlattices. The FOM of these HMMs outperforms those of state-of-the-art AZO/ZnO based HMMs above 1.8 µm. Interestingly, LSTO/STO superlattices are hyperbolic from 1.46 to 4.5 µm, in a range where no hyperbolic material was available so far, which opens attractive perspectives for telecom and military applications. Besides, the hyperbolic range and the dielectric properties of LSTO based HMMs can be conveniently tuned by changing the La concentration. The thicknesses of the individual STO and LSTO layers forming these HMMs is very small, in the few nm range. This is a remarkable feature leveraging very compact

integration in photonic devices. Our results also suggest that the very low thicknesses of the STO insulating layers may promote coupling between the surface plasmons localized at the STO/LSTO interfaces, which affects the HMMs response. This may be opportunely exploited as a new degree of freedom to engineer the HMMs response. In addition, LSTO/STO based HMMs are single crystalline and epitaxial, and composed of chemically homogeneous oxide layers liable to be etched in a single step with a unique process. This is expected to ease their patterning as compared to classical HMMs where different etching process are required to structure the metal and the dielectric layers. This is all the more attractive for application in photonic hypercrystals, made of photonic crystals patterns transferred to HMMs, to control light-matter interaction.[57] Transferring patterns in HMMs has also been recently reported as a promising path towards the control of both their electric permittivity and magnetic permeability and to the demonstration of magnetic hyperbolic dispersion, opening new opportunities for photonic and magnetic applications.[58] In the end, as they are epitaxial, LSTO/STO HMMs can be combined by epitaxy to the many members of the functional oxide family, opening the perspective of their integration in multifunctional heterostructures and devices. They can also be grown on Si and GaAs technological platforms by epitaxy using STO/Si[59,60] and STO/GaAs[61,62] templates, making them perfectly suited for flexible integration in nanophotonic devices.

Methods

The samples were grown by oxide-molecular beam epitaxy (MBE) on non-intentionally doped STO substrates. Before growth, untreated substrates were introduced in the reactor and annealed at 550°C during 30 min under a di-oxygen partial pressure $P(O_2)$ of 10^{-7} Torr. Sr, Ti, and if appropriate La were codeposited from Knudsen effusion cells at this temperature and under this partial pressure, at a growth rate of approximately 1 to 2 monolayers (ML) per minute. Flux where

calibrated by combining Bayard-Alpert gauge, X-ray reflectivity (to determine thicknesses) and X-ray photoemission spectroscopy (to determine compositions) in order to control thicknesses and compositions. After growth, the samples were annealed under air in a tubular furnace at 450°C for 1h. The structural properties of the samples were analyzed by X-ray diffraction (XRD) using a Rigaku Smartlab diffractometer equipped with a rotating anode and high resolution optics (two bounces Ge(220) monochromator combined with variable aperture slits and Soller collimators). The dielectric functions were measured by variable angle ellipsometry using a Horiba Jobin-Yvon Uvisel ellipsometer. Oscillator models where used to extract permittivity dispersions from ellipsometric angles measurements. The ellipsometer enables measurements in the 0.59 to 4.76 eV (0.26 to 2.1 µm) range. The results presented outside this range in Fig.3 and 4 where extrapolated using the oscillator models used to fit the ellipsometric data in the measurement range. The procedure is detailed in the Supplementary Information.

AUTHOR INFORMATION

Corresponding Author

*Corresponding author: guillaume.saint-girons@ec-lyon.fr

Author Contributions

The manuscript was written through contributions of all authors. All authors have given approval to the final version of the manuscript.

Funding Sources

This work was partially supported by the French ANR projects LILIT (grant # ANR-16-CE24-0022), MITO (grant # ANR-17-CE05-0018-01) and DIAMWAFEL (grant # ANR-15-CE08-0034-02)

ACKNOWLEDGMENT

The authors gratefully thank Philippe Regreny, Claude Botella and Jean-Baptiste Goure for technical support.

ASSOCIATED CONTENT

Supporting Information : details of the structural and ellipsometry measurements and associated analyses

REFERENCES

(1) Wong, Z. J.; Wang, Y.; O'Brien, K.; Rho, J.; Yin, X.; Zhang, S.; Fang, N.; Yen, T.-J.; Zhang, X. Optical and Acoustic Metamaterials: Superlens, Negative Refractive Index and Invisibility Cloak. *J. Opt.* **2017**, *19*, 084007.

(2) Sun, J.; Litchinitser, N. M.; Zhou, J. Indefinite by Nature: From Ultraviolet to Terahertz. *ACS Photonics* **2014**, *1*, 293–303.

(3) Yao, J.; Liu, Z.; Liu, Y.; Wang, Y.; Sun, C.; Bartal, G.; Stacy, A. M.; Zhang, X. Optical Negative Refraction in Bulk Metamaterials of Nanowires. *Science* **2008**, *321*, 930–930.

(4) Xiong, Y.; Liu, Z.; Sun, C.; Zhang, X. Two-Dimensional Imaging by Far-Field Superlens at Visible Wavelengths. *Nano Lett.* **2007**, *7*, 3360–3365.

(5) Yang, X.; Yao, J.; Rho, J.; Yin, X.; Zhang, X. Experimental Realization of Three-Dimensional Indefinite Cavities at the Nanoscale with Anomalous Scaling Laws. *Nat. Photonics* **2012**, *6*, 450–454.

(6) Noginov, M. A.; Li, H.; Barnakov, Y. A.; Dryden, D.; Nataraj, G.; Zhu, G.; Bonner, C. E.; Mayy, M.; Jacob, Z.; Narimanov, E. E. Controlling Spontaneous Emission with Metamaterials. *Opt. Lett.* **2010**, *35*, 1863.

(7) Biehs, S.-A.; Tschikin, M.; Ben-Abdallah, P. Towards a Black Body for Near-Field Thermal Radiation. **2011**, *104301*, 1–5.

(8) Poddubny, A.; Iorsh, I.; Belov, P.; Kivshar, Y. Hyperbolic Metamaterials. *Nat. Photonics* **2013**, *7*, 958–967.

(9) Boltasseva, A.; Atwater, H. A. Low-Loss Plasmonic Metamaterials. *Science* **2011**, *331*, 290–291.

(10) Naik, G. V.; Shalaev, V. M.; Boltasseva, A. Alternative Plasmonic Materials: Beyond Gold and Silver. *Adv. Mater.* **2013**, *25*, 3264–3294.

(11) Eich, M.; Lang, S.; Ritter, M.; Lee, H. S.; Störmer, M.; Petrov, A. Y. Gold-Silicon Metamaterial with Hyperbolic Transition in near Infrared. *Appl. Phys. Lett.* **2013**, *103*, 021905.

(12) Drachev, V. P.; Chettiar, U. K.; Kildishev, A. V.; Yuan, H.-K.; Cai, W.; Shalaev, V. M. The Ag Dielectric Function in Plasmonic Metamaterials. *Opt. Express* **2008**, *16*, 1186.

(13) Caldwell, J. D.; Kretinin, A. V.; Chen, Y.; Giannini, V.; Fogler, M. M.; Francescato, Y.; Ellis, C. T.; Tischler, J. G.; Woods, C. R.; Giles, A. J.; et al. Sub-Diffractional Volume-Confined Polaritons in the Natural Hyperbolic Material Hexagonal Boron Nitride. *Nat. Commun.* **2014**, *5*, 5221.

(14) Esslinger, M.; Vogelgesang, R.; Talebi, N.; Khunsin, W.; Gehring, P.; de Zuani, S.; Gompf, B.; Kern, K. Tetradymites as Natural Hyperbolic Materials for the Near-Infrared to Visible. *ACS Photonics* **2014**, *1*, 1285–1289.

(15) West, P. R.; Ishii, S.; Naik, G. V.; Emani, N. K.; Shalaev, V. M.; Boltasseva, A. Searching for Better Plasmonic Materials. *Laser Photonics Rev.* **2010**, *4*, 795–808.

(16) Johnson, P. B.; Christy, R. W. Optical Constants of the Noble Metals. *Phys. Rev. B* **1972**, *6*, 4370–4379.

(17) Hoffman, A. J.; Alekseyev, L.; Howard, S. S.; Franz, K. J.; Wasserman, D.; Podolskiy, V. A.; Narimanov, E. E.; Sivco, D. L.; Gmachl, C. Negative Refraction in Semiconductor Metamaterials. *Nat. Mater.* **2007**, *6*, 946–950.

(18) Chang, Y.-C.; Liu, C.-H.; Liu, C.-H.; Zhang, S.; Marder, S. R.; Narimanov, E. E.; Zhong, Z.; Norris, T. B. Realization of Mid-Infrared Graphene Hyperbolic Metamaterials. *Nat. Commun.* **2016**, *7*, 12568.

(19) Naik, G. V.; Kim, J.; Boltasseva, A. Oxides and Nitrides as Alternative Plasmonic Materials in the Optical Range [Invited]. *Opt. Mater. Express* **2011**, *1*, 1090.

(20) Naik, G. V.; Boltasseva, A. A Comparative Study of Semiconductor-Based Plasmonic Metamaterials. *Metamaterials* **2011**, *5*, 1–7.

(21) Guo, Y.; Cortes, C. L.; Molesky, S.; Jacob, Z. Broadband Super-Planckian Thermal Emission from Hyperbolic Metamaterials. *Appl. Phys. Lett.* **2012**, *101*, 131106.

(22) Naik, G. V.; Schroeder, J. L.; Ni, X.; Kildishev, A. V.; Sands, T. D.; Boltasseva, A. Titanium Nitride as a Plasmonic Material for Visible and Near-Infrared Wavelengths. *Opt. Mater. Express* **2012**, *2*, 478.

(23) Walukiewicz, W. Intrinsic Limitations to the Doping of Wide-Gap Semiconductors. *Phys. B Condens. Matter* **2001**, *302–303*, 123–134.

(24) Neave, J. H.; Dobson, P. J.; Harris, J. J.; Dawson, P.; Joyce, B. A. Silicon Doping of MBE-Grown GaAs Films. *Appl. Phys. A Solids Surfaces* **1983**, *32*, 195–200.

(25) *III-V Integrated Circuit Fabrication Technology*; Tiku, S., Biswas, D., Eds.; Pan Stanford, 2016. https://doi.org/10.1201/b19367

(26) Yamada, T.; Tokumitsu, E.; Saito, K.; Akatsuka, T.; Miyauchi, M.; Konagai, M.; Takahashi, K. Heavily Carbon Doped P-Type GaAs and GaAlAs Grown by Metalorganic Molecular Beam Epitaxy. *J. Cryst. Growth* **1989**, *95*, 145–149.

(27) Jalan, B.; Stemmer, S. Large Seebeck Coefficients and Thermoelectric Power Factor of La-Doped $SrTiO_3$ Thin Films. *Appl. Phys. Lett.* **2010**, *97*, 042106.

(28) Apreutesei, M.; Debord, R.; Bouras, M.; Regreny, P.; Botella, C.; Benamrouche, A.; Carretero-Genevrier, A.; Gazquez, J.; Grenet, G.; Pailhès, S.; et al. Thermoelectric La-Doped $SrTiO_3$ Epitaxial Layers with Single-Crystal Quality: From Nano to Micrometers. *Sci. Technol. Adv. Mater.* **2017**, *18*, 430–435.

(29) Ravichandran, J.; Siemons, W.; Heijmerikx, H.; Huijben, M.; Majumdar, A.; Ramesh, R. An Epitaxial Transparent Conducting Perovskite Oxide: Double-Doped $SrTiO_3$. *Chem. Mater.* **2010**, *22*, 3983–3987.

(30) Son, J.; Moetakef, P.; Jalan, B.; Bierwagen, O.; Wright, N. J.; Engel-Herbert, R.; Stemmer, S. Epitaxial SrTiO3 Films with Electron Mobilities Exceeding 30,000 $Cm^2xV^{-1}xS^{-1}$. *Nat. Mater.* **2010**, *9*, 482–484.

(31) Okuda, T.; Nakanishi, K.; Miyasaka, S.; Tokura, Y. Large Thermoelectric Response of Metallic Perovskites. *Phys. Rev. B* **2001**, *63*, 113104.

(32) Choi, M.; Posadas, A. B.; Rodriguez, C. A.; O'Hara, A.; Seinige, H.; Kellock, A. J.; Frank, M. M.; Tsoi, M.; Zollner, S.; Narayanan, V.; et al. Structural, Optical, and Electrical Properties of Strained La-Doped $SrTiO_3$ Films. *J. Appl. Phys.* **2014**, *116*, 043705.

(33) Choi, W. S.; Yoo, H. K.; Ohta, H. Polaron Transport and Thermoelectric Behavior in La-Doped $SrTiO_3$ Thin Films with Elemental Vacancies. *Adv. Funct. Mater.* **2015**, *25*, 799–804.

(34) Cain, T. A.; Kajdos, A. P.; Stemmer, S. La-Doped $SrTiO_3$ Films with Large Cryogenic Thermoelectric Power Factors. *Appl. Phys. Lett.* **2013**, *102*, 182101.

(35) Ravichandran, J.; Siemons, W.; Oh, D.-W.; Kardel, J. T.; Chari, A.; Heijmerikx, H.; Scullin, M. L.; Majumdar, A.; Ramesh, R.; Cahill, D. G. High-Temperature Thermoelectric Response of Double-Doped $SrTiO_3$ Epitaxial Films. *Phys. Rev. B* **2010**, *82*, 165126.

(36) Seo, S. S. A.; Han, M. J.; Hassink, G. W. J.; Choi, W. S.; Moon, S. J.; Kim, J. S.; Susaki, T.; Lee, Y. S.; Yu, J.; Bernhard, C.; et al. Two-Dimensional Confinement of 3d1 electrons in $LaTiO_3/LaAlO_3$ multilayers. *Phys. Rev. Lett.* **2010**, *104*, 036401.

(37) Keeble, D. J.; Jalan, B.; Ravelli, L.; Egger, W.; Kanda, G.; Stemmer, S. Suppression of Vacancy Defects in Epitaxial La-Doped $SrTiO_3$ Films. *Appl. Phys. Lett.* **2011**, *99*, 232905.

(38) Janotti, A.; Jalan, B.; Stemmer, S.; Van de Walle, C. G. Effects of Doping on the Lattice Parameter of $SrTiO_3$. *Appl. Phys. Lett.* **2012**, *100*, 262104.

(39) Wiff, J. P.; Kinemuchi, Y.; Watari, K. Hall Mobilities of Al- and Ga-Doped ZnO Polycrystals. *Mater. Lett.* **2009**, *63*, 2470–2472.

(40) Liu, H.; Avrutin, V.; Izyumskaya, N.; Özgür, Ü.; Morkoç, H. Transparent Conducting Oxides for Electrode Applications in Light Emitting and Absorbing Devices. *Superlattices Microstruct.* **2010**, *48*, 458–484.

(41) Pradhan, A. K.; Mundle, R. M.; Santiago, K.; Skuza, J. R.; Xiao, B.; Song, K. D.; Bahoura, M.; Cheaito, R.; Hopkins, P. E. Extreme Tunability in Aluminum Doped Zinc Oxide Plasmonic Materials for Near-Infrared Applications. *Sci. Rep.* **2015**, *4*, 6415.

(42) I. F. Almog and M. S. Bradley and V. Bulovi´c, 2011. The Lorentz Oscillator and its applications, MITOpenCourseWare.

(43) *Principle of Optics*; Born, M., Wolf, E., Cambridge University Press, 1999. ISBN : 0-521-63921-2

(44) Apell, P.; Hunderi, O.; Monreal, R. Superlattice Optics. *Physica Scripta* **1986**, *34*, 348-352

(45) Agranovich, V.M.; Kravtsov, V.E. Superlattice Optics. *Notes on Crystal Optics for Superlattices* **1985**, *55*, 85-90

(46) Drachev, V. P.; Podolskiy, V. A.; Kildishev, A. V. Hyperbolic Metamaterials: New Physics behind a Classical Problem. *Opt. Express* **2013**, *21*, 15048.

(47) Wangberg, R.; Elser, J.; Narimanov, E. E.; Podolskiy, V. A. Nonmagnetic Nanocomposites for Optical and Infrared Negative-Refractive-Index Media. *J. Opt. Soc. Am. B* **2006**, *23*, 498.

(48) Rytov, S. M.; Electromagnetic Properties of a Finely Stratified Medium. *Sov. Phys. JETP* **1956**, *2*, 466

(49) Cardona, M. Optical Properties and Band Structure of $SrTiO_3$ and $BaTiO_3$. *Phys. Rev.* **1965**, *140,* A651.

(50) Wunderlich, W.; Ohta, H.; Koumoto, K. Enhanced Effective Mass in Doped $SrTiO_3$ and Related Perovskites. **2009**, *404*, 2202–2212.

(51) Bouzerar, G.; Thébaud, S.; Bouzerar, R.; Pailhès, S.; Adessi, Ch. Absence of Confinement in $(SrTiO_3)/(SrTi_{0.8}Nb_{0.2}O_3)$ superlattices. *Phys. Rev. Materials.* **2018**, *2*, 035402.

(52) Eich, M.; Lang, S.; Ritter, M.; Lee, H. S.; Störmer, M.; Petrov, A. Y. Gold-Silicon Metamaterial with Hyperbolic Transition in near Infrared. *Appl. Phys. Lett.* **2013**, *103*, 021905.

(53) Saha, B.; Naik, G. V.; Saber, S.; Akatay, C.; Stach, E. A.; Shalaev, V. M.; Boltasseva, A.; Sands, T. D. TiN/(Al,Sc)N Metal/Dielectric Superlattices and Multilayers as Hyperbolic Metamaterials in the Visible Spectral Range. *Phys. Rev. B* **2014**, *90*, 125420.

(54) Naik, G. V.; Liu, J.; Kildishev, A. V.; Shalaev, V. M.; Boltasseva, A. Demonstration of Al:ZnO as a Plasmonic Component for near-Infrared Metamaterials. *Proc. Natl. Acad. Sci.* **2012**, *109*, 8834–8838.

(55) Kalusniak, S.; Orphal, L.; Sadofev, S. Demonstration of Hyperbolic Metamaterials at Telecommunication Wavelength Using Ga-Doped ZnO. *Opt. Express* **2015**, *23*, 32555.

(56) Mihalcea, R. M.; Webber, M. E.; Baer, D. S.; Hanson, R. K.; Feller, G. S.; Chapman, W. B. Diode-Laser Absorption Measurements of CO 2 , H 2 O, N 2 O, and NH 3 near 2.0 Mm. *Appl. Phys. B Lasers Opt.* **1998**, *67*, 283–288.

(57) Galfsky, T.; Gu, J.; Narimanov, E. E.; Menon, V. M. Photonic Hypercrystals for Control of Light–matter Interactions. *Proc. Natl. Acad. Sci.* **2017**, *114*, 5125–5129.

(58) Kruk, S. S.; Wong, Z. J.; Pshenay-Severin, E.; O'Brien, K.; Neshev, D. N.; Kivshar, Y. S.; Zhang, X. Magnetic Hyperbolic Optical Metamaterials. *Nat. Commun.* **2016**, *7*, 11329.

(59) McKee, R. A.; Walker, F. J.; Chisholm, M. F. Crystalline Oxides on Silicon: The First Five Monolayers. *Phys. Rev. Lett.* **1998**, *81*, 3014–3017.

(60) Saint-Girons, G.; Bachelet, R.; Moalla, R.; Meunier, B.; Louahadj, L.; Canut, B.; Carretero-Genevrier, A.; Gazquez, J.; Regreny, P.; Botella, C.; et al. Epitaxy of $SrTiO_3$ on Silicon: The Knitting Machine Strategy. *Chem. Mater.* **2016**, *28*, 5347–5355.

(61) Liang, Y.; Kulik, J.; Eschrich, T. C.; Droopad, R.; Yu, Z.; Maniar, P. Hetero-Epitaxy of Perovskite Oxides on GaAs(001) by Molecular Beam Epitaxy. *Appl. Phys. Lett.* **2004**, *85*,

(62) Louahadj, L.; Le Bourdais, D.; Largeau, L.; Agnus, G.; Mazet, L.; Bachelet, R.; Regreny, P.; Albertini, D.; Pillard, V.; Dubourdieu, C.; et al. Ferroelectric $Pb(Zr,Ti)O_3$ Epitaxial Layers on GaAs. *Appl. Phys. Lett.* **2013**, *103*, 212901.

TABLE OF CONTENTS GRAPHIC

For table of contents use only

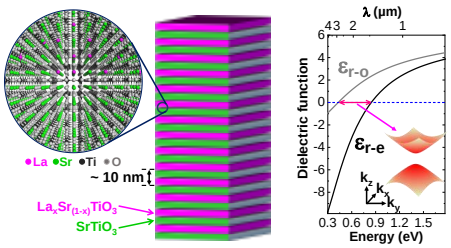

Perovskite-oxide based hyperbolic metamaterials

Mohamed Bouras, Dong Han, Sébastien Cueff, Romain Bachelet and Guillaume Saint-Girons

Synopsis : Perovskite oxide based hyperbolic epitaxial metamaterial made of a $SrTiO_3/La_xSr_{(1-x)}TiO_3$ superlattice, showing hyperbolic dispersion in the near- to mid-infrare region.